Chinese Chemical Letters 35 (2024) 109326

Contents lists available at ScienceDirect

Chinese Chemical Letters

journal homepage: www.elsevier.com/locate/cclet

Manganese vanadium oxide composite as a cathode for high-performance aqueous zinc-ion batteries

Jiayu Bai[a], Songjie Hu[a], Lirong Feng[a], Xinhui Jin[a], Dong Wang[a], Kai Zhang[b], Xiaohui Guo[a,*]

[a] Key Lab of Synthetic and Natural Functional Molecule Chemistry of Ministry of Education, Shaanxi Key Laboratory for Carbon Neutral Technology, The College of Chemistry and Materials Science, Northwest University, Xi'an 710069, China
[b] Sustainable Materials and Chemistry, Dept. Wood Technology and Wood-based Composites, University of Goettingen, Wilhelmsplatz 1 (Aula) 37073 Göttingen, Germany

ARTICLE INFO

Article history:
Received 11 September 2023
Revised 15 October 2023
Accepted 21 November 2023
Available online 25 November 2023

Keywords:
Metal organic framework
Manganese oxides
Heterostructure
Cathode
Zinc ion battery

ABSTRACT

The development of clean renewable energy and energy storage devices is of great significance under the present energy crisis and environmental pollution background. Aqueous zinc-ion battery (ZIB) has become one of the most promising energy storage devices due to its high capacity, safety and low cost. However, the application of ZIB cathode is usually limited by low capacity and poor stability. Herein, we propose a novel heterostructure MnO/MnV_2O_4 composite material composed of MOF derivatives and spinel with dual active components as cathode for ZIBs. Benefited from substantial framework of MOF derivatives and the synergistic effect of heterostructures, MnO/MnV_2O_4 exhibits excellent rate performance (342 mAh/g at 0.1 A/g, 261 mAh/g at 15 A/g) and cycling performance (198.9 mAh/g at 10 A/g after 2000 cycles) in 3 mol/L $Zn(CF_3SO_3)_2$ electrolytes. This work extends the range of developing high-performance cathodes for ZIBs under high current density and is expected to enlighten the optimization of commercial energy storage devices.

As environmental pollution aggravates and energy supply-demand contradiction intensifies, it is urgent to develop renewable energy [1–6]. However, most renewable energy sources are easily limited by time, region and other specific conditions, resulting in an inability to provide a constant and steady supply of energy [7–9]. Therefore, it is necessary to develop safe and efficient energy storage and conversion technologies [10–13]. Lithium-ion battery (LIB) is one of the relatively mature commercial electrochemical energy storage devices [14–16]. However, limited by numerous factors including toxic and flammable electrolyte, high cost as well as lack of lithium resources, the further development of LIBs is relatively difficult to achieve long-term applications [17–20]. It is noted that, aqueous rechargeable battery becomes one of promising storage devices due to avoiding a series of safety concerns and reduced assembly conditions and manufacturing costs. In addition, the conductivity of aqueous electrolyte (0.1–1 S/cm) is higher than that of organic electrolyte (10^{-3}–10^{-2} S/cm), which accelerates ion transport [17,19,21-25].

To date, a variety of aqueous metal ion batteries have been studied. Study indicated that it is easier for multivalent metal ion batteries to exhibit higher discharge capacity and energy density due to the participation of multiple electrons in the reaction process [12,19,26,27]. However, most of multivalent metal batteries do not work normally in aqueous electrolyte because of strong interaction between multivalent cations and electrode materials as well as acute passivation on the anode surface [19,28-31]. Unlike other metals, high redox potential of Zn (−0.76 V *vs.* SHE) suppresses the evolution of H_2, allowing battery to work securely and stably in aqueous electrolyte. Besides, ZIB exhibits high theoretical volumetric (5855 mAh/cm^3) and gravimetric capacity (820 mAh/g), smaller ion radius for faster ion insertion/extraction, abundant reserves and low cost [4,23,32-36]. Herein, manganese-based compounds and vanadium-based compounds are the most widely studied cathode materials. Manganese-based compounds possess high theoretical capacity and working voltage, but dissolution of Mn and lattice distortion and disproportionation caused by Jahn-Teller effect, results in rapid capacity decay and poor rate performance [33,36-39]. Vanadium-based compounds exhibit moderate capacity and better capability, while their average working voltage is in dire of boost [14,40,41].

* Corresponding author.
E-mail address: guoxh2009@nwu.edu.cn (X. Guo).

https://doi.org/10.1016/j.cclet.2023.109326
1001-8417/

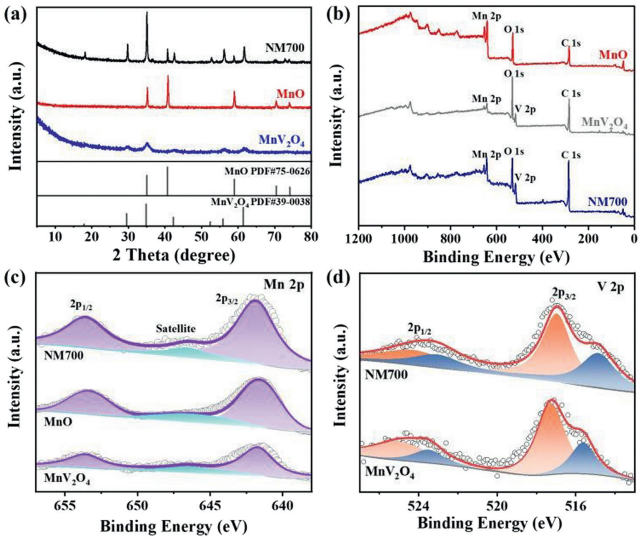

Fig. 1. (a) XRD patterns of NM700, MnO and MnV_2O_4. (b) XPS survey spectrum of NM700, MnO and MnV_2O_4. (c, d) High-resolution XPS spectrum of Mn 2p, and V 2p respectively in the resulting NM700, MnO and MnV_2O_4.

Here, to address the structural collapse and poor conductivity of manganese oxides during charge and discharge process, we prepared manganese oxides by annealing manganese-based metal organic framework (MOF), meanwhile, it is a feasible choice for achieving wider working voltage window and better rate performance by combining manganese oxides and vanadium oxides in a sensible way. Additionally, binary metal oxides exhibit excellent electrochemical activity due to high electronic conductivity and polyvalent states of two transition metals.

Inspired by the above issues, we present a novel heterostructure MnO/MnV_2O_4 composite material (NM700) composed of MOF derivatives and spinel with dual active components. MOF derivatives provide robust structure support, heterostructures generate abundant interfaces to accelerate charge transfer, and combine respective advantages of MnO and MnV_2O_4, thus enabling composite material with excellent rate performance and robust cycle stability.

The typical XRD patterns of NM700, MnO and MnV_2O_4 samples are displayed in Fig. 1a. The XRD patterns of NM700 were well-assigned to the cubic phase of MnO (PDF#75–0626) and the face-center cubic phase of MnV_2O_4 (PDF#39–0038). The diffraction peaks at 35.0°, 40.6°, 58.8°, 70.3° and 73.9° of NM700 are corresponding to (111), (200), (220), (311) and (222) planes of MnO phase, respectively. While the diffraction peaks at 17.9°, 29.5°, 34.8°, 42.3°, 52.4°, 55.9° and 61.4° of NM700 are corresponding to (111), (220), (311), (400), (422), (333) and (440) planes of MnV_2O_4 phase, respectively. The results of XRD confirm the formation of composite phases in NM700. Besides, the XRD patterns of MnO are in accordance with standard MnO (PDF#75–0626), and the diffraction peaks of MnV_2O_4 are well assigned to standard MnV_2O_4 (PDF #39–0038).

XPS analysis is generally used to identify the element composition and valence state of samples. Fig. 1b presents XPS survey spectrum of NM700, MnO and MnV_2O_4, further identifying the presence of Mn, V, C and O elements on the surface of NM700. The Mn 2p spectrum of NM700 in Fig. 1c shows two main peaks centered at 641.8 and 653.5 eV corresponding to Mn $2p_{3/2}$ and Mn $2p_{1/2}$ of Mn^{2+}, and the satellite peak at 646.5 eV also reveals the presence of Mn^{2+} [42]. The peaks of Mn 2p is positively shifted towards higher binding energy compared to MnO (641.5 eV/653.3 eV), indicating the lower electron density of Mn^{2+} in NM700 (MnO/MnV_2O_4). The opposite happens to V 2p, the V 2p

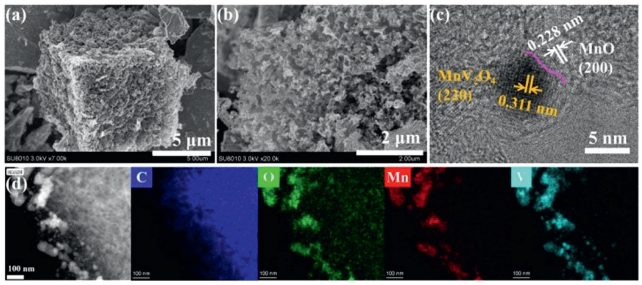

Fig. 2. (a, b) SEM images, (c) TEM image and (d) HADDF and elemental mapping images of NM700.

spectrum of MnV_2O_4 in Fig. 1d can be distinguished as V^{3+} ($2p_{3/2}$, 515.6 eV; $2p_{1/2}$, 523.4 eV) and V^{5+} ($2p_{3/2}$, 517.3 eV; $2p_{1/2}$, 524.8 eV) [43]. It is obviously that V 2p peaks of NM700 (514.9 eV/523.0 eV, 516.9 eV/524.2 eV) are negatively shifted towards lower binding energy compared to MnV_2O_4, which demonstrates an inflow of electrons in V element of MnO/MnV_2O_4. Therefore, it was deduced that the formation of an internal electric field caused by heterostructure leads to the flow of electrons from MnO to MnV_2O_4 [44]. The high-resolution C 1s spectrum (Fig. S1a in Supporting information) displays that there are two peaks at 284.8 and 285.7 eV, corresponding to C–C and C=O, respectively [42]. And the O 1s spectrum of NM700 (Fig. S1b in Supporting information) can be divided into two peaks at 530.4 and 531.5 eV, which are attributed to M-O (M = metal) and C–O, respectively [45].

In Fig. 2a, the SEM image of as-prepared NM700 exhibits a typical cube, which inherits the original morphology of Mn-MOF precursor (Fig. S2 in Supporting information). It also can be observed that the surface of NM700 is rough and porous (Fig. 2b). As shown in Fig. S2, Mn-MOF displays a cubic structure with a smooth surface. MnO prepared by calcining Mn-MOF at 700 °C exhibits a cubic structure similar to Mn-MOF. The uneven surface of MnO with many pores can be clearly observed in Fig. S3 (Supporting information). The morphology of MnV_2O_4 signifies irregularly shaped blocks with smooth surface (Fig. S4 in Supporting information).

The TEM images in Fig. S5 (Supporting information) show that NM700 is consisted of stacked nanoparticles with a mean diameter of less than 100 nm, and there should be a layer of amorphous carbon on the surface of NM700, which probably originates from the decomposition of the MOF ligand, upgrading the inherent low electronic conductivity of manganese oxide and vanadium oxide materials. From the TEM image of NM700 in Fig. 2c, in addition, the observed lattice spacings of 0.228 nm and 0.311 nm are attributed to (200) plane of the MnO and (220) plane of the MnV_2O_4, respectively, which are well matched with the results of XRD. In the meantime, the above results manifest the existence of MnO/MnV_2O_4 heterostructure. Additionally, elemental mapping images demonstrate that C, O, Mn and V elements are distributed uniformly throughout the NM700 (Fig. 2d).

The N_2 adsorption-desorption isotherm of NM700 is shown in Fig. S6a (Supporting information). The BET specific surface area of NM700 is measured to be 114.50 m^2/g, and the average pore size of NM700 is 5.26 nm (Fig. S6b in Supporting information). Abundant pores and the hierarchical pore structure with micropore and mesopore facilitate ion diffusion and also macropore provides buffer space for ion insertion. The metal element content of NM700 was determined by ICP-MS (Table S1 in Supporting information). The results exhibit that the atomic ratio of Mn to V in NM700 is 0.677:1. From this, it is deduced that the molar ratio of MnO and MnV_2O_4 components in NM700 is 0.353:1.

To evaluate the electrochemical performance of NM700 as cathode materials in ZIBs, the Zn//NM700 battery was assembled and

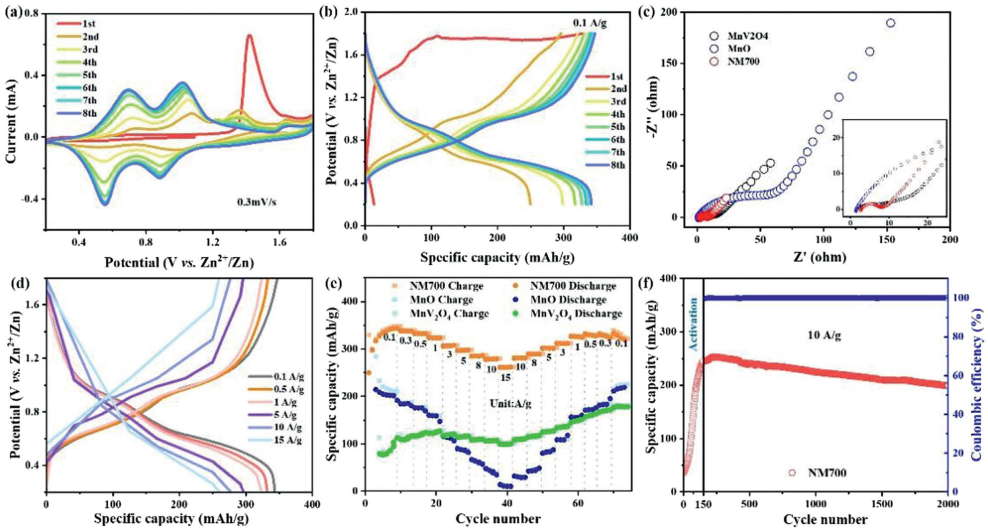

Fig. 3. Electrochemical performance of the NM700 cathode. (a) CV curves of the 1st-8th cycles at the scan rate of 0.3 mV/s. (b) Galvanostatic charge-discharge (GCD) curves during different cycles at the current density of 0.1 A/g for NM700. (c) Nyquist plots after CV activation of NM700, MnO and MnV_2O_4. (d) GCD curves at current density from 0.1 A/g to 15 A/g of NM700. (e) Rate performance at current density from 0.1 A/g to 15 A/g of NM700, MnO and MnV_2O_4. (f) Long-term cycling performance of NM700 at 10 A/g.

tested. Fig. 3a shows cyclic voltammogram (CV) curves of the initial eight cycles at a scan rate of 0.3 mV/s over a voltage range of 0.2–1.8 V (*vs.* Zn^{2+}/Zn). For the first charge process, the significant oxidation peak at 1.42 V appears and vanishes gradually in the following cycles, corresponding to the occurrence of an irreversible reaction at 1.42 V. With the increasing of the cycle numbers, the area of CV curve becomes larger than that of the former, which means an increase of the electrochemical capacity and the activation of NM700. Furthermore, the CV curves of the sixth to the eighth cycles are basically overlapped, which indicates that the electrochemical reaction is highly reversible after the initial activation process.

The galvanostatic charge–discharge (GCD) curves of NM700 are consistent with the result of CV curves (Fig. 3b). It appears a long plateau region corresponding to an irreversible phase transformation in the first charge curve. The subsequent discharge and charge curves are consisted of two slope plateaus, reflecting the solid-solution reaction associated with the insertion/extraction of Zn^{2+} and H^+ [46]. After activating at the current density of 0.1 A/g in the initial cycles, the specific capacities of the first to eighth cycles are rapidly increased from 13.45 mAh/g to 342.85 mAh/g, indicating that the reconstructed structure is more conducive to Zn^{2+} storage during the irreversible phase transition. According to previous research, the phase transition may be the amorphization of MnV_2O_4, which form an amorphous phase with enriched sites can play a significant buffering role in subsequent reactions [47].

Nyquist plots are generally used to evaluate the impedance values of electrode materials in different states. The semicircle of the high frequency region represents the charge transfer resistance of the electrode, meanwhile, the smaller semicircle radius corresponds to the smaller impedance, which is more beneficial for charge transfer. The semicircle radius of NM700 is smaller than that of MnO and MnV_2O_4 in Fig. 3c, verifying that MnO/MnV_2O_4 heterostructure can generate abundant active sites that accelerate ion diffusion and charge transfer processes.

Furthermore, the rate performance of NM700 electrode was evaluated at different current densities ranging from 0.1 A/g to 15 A/g (Figs. 3d and e). When the current density varies from 0.1 A/g to 0.5, 1, 5, 10 and 15 A/g, the discharge specific capacities are 342, 332, 323, 297, 279 and 261 mAh/g, respectively (Fig. 3d). Interestingly, the capacity is decreased by only 23% when the current density increases from 0.1 A/g to 15 A/g, which is attributed to the specific heterostructure inheriting high capacity of MnO and outstanding rate performance of MnV_2O_4. As it returns to 0.1 A/g, discharge specific capacity is up to approximately 328 mAh/g, indicating good reversibility and excellent rate performance (Fig. 3e). In contrast, MnO exhibits large capacities at the low current density but capacities attenuate severely at the high current density (11 mAh/g at 15 A/g), while MnV_2O_4 presents less capacity loss but low capacities (178 mAh/g at 0.1 A/g).

To evaluate the cycling stability of NM700 in depth, long-term cycling test was conducted at a higher current density of 10 A/g (Fig. 3f). Impressively, the capacity of NM700 was increased to 245.5 mAh/g during the first 150th cycles of the cathode activation process. After 2000th cycles, a large specific capacity of 198.9 mAh/g (81.0%) is still retained with a coulombic efficiency of almost 100%, while the specific capacity of MnO and MnV_2O_4 are only 53.3 and 141.6 mAh/g, respectively (Fig. S7 in Supporting information), which further demonstrates that NM700 possesses high reversible capacity and excellent cycling stability even under high current density. Table S2 (Supporting information) shows the comparison of the rate and cycling performance of recently reported manganese-based and vanadium-based materials. Compared with the above materials, MnO/MnV_2O_4 exhibits optimal specific capacity and cycling stability at high current density, indicating the potential application prospects of MnO/MnV_2O_4 cathode material in ZIBs.

To further explore Zn^{2+} storage behavior of NM700, it was investigated the electrochemical kinetics in the Zn//NM700 cell. Fig. 4a exhibits CV curves range from 0.3 mV/s to 1.5 mV/s of NM700, and the shape of CV curves can maintain almost consistent at different scan rates. The storage mechanism can be evaluated by the following formula.

$$i = av^b \tag{1}$$

Here, i represents the peak current, v represents the scan rate, a and b are variate coefficients. The value of b can be calculated by Eq. 2 converted from Eq. 1.

$$\log(i) = b \times \log(v) + \log(a) \tag{2}$$

When the value of b approaches to 1, it implies that the electrochemical process is dominated by the surface capacitive behavior;

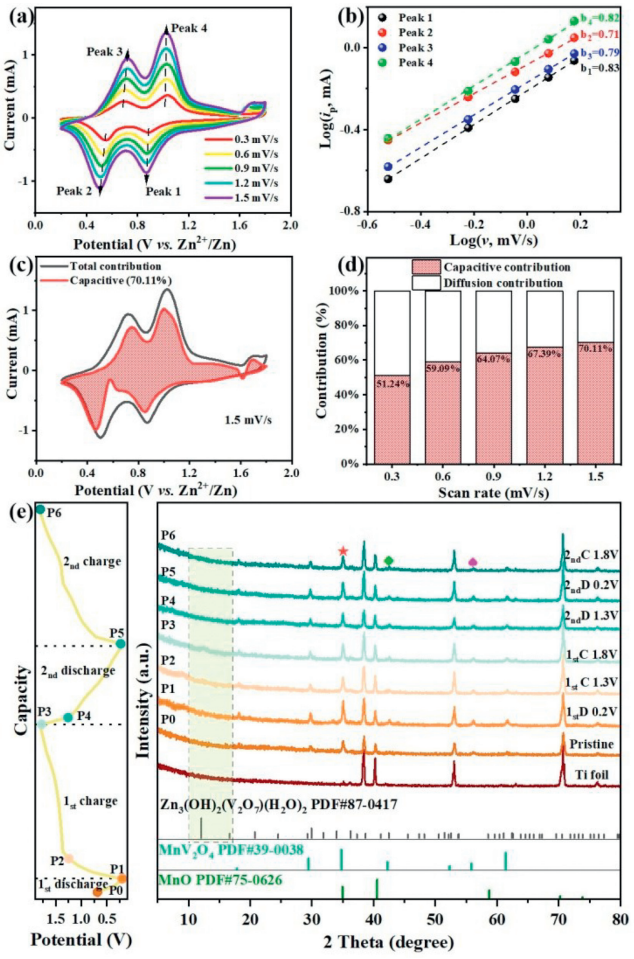

Fig. 4. (a) CV curves at different scan rates. (b) log(*i*, current) and log(*v*, scan rate) plots at specific peak currents. (c) The capacitive contribution at 1.5 mV/s. (d) The contribution rate of capacitive capacities to total charge storage at different scan rates. (e) *Ex situ* XRD patterns of NM700 during the first and second discharge/charge cycles at 0.1 A/g.

when the value of *b* approaches to 0.5, it implies that the electrochemical process is dominated by the ion diffusion behavior. As shown in Fig. 4b, the *b* values of redox peaks in NM700 are 0.83, 0.71, 0.79 and 0.82, which illustrates that the electrochemical reaction process is jointly controlled by diffusion and capacitive behavior, and capacitive process plays a major role in the electrochemical reaction.

According to Eq. 3, the k_1v is calculated, which means the contribution part of capacitive capacities at specific scan rates. Fig. 4c shows that the capacitive proportion (red region) is determined to be 70.11% in the CV curve at a scan rate of 1.5 mV/s based on Eq. 3. The contribution rate of capacitive capacities to total charge storage in NM700 are portrayed in Fig. 4d, they are 51.24%, 59.09%, 64.07%, 67.39% and 70.11% at the scan rate of 0.3, 0.6, 0.9, 1.2 and 1.5 mV/s respectively, implying that capacitive process gradually dominates kinetic process of NM700 with the scan rate increasing.

$$i(V) = k_1 v + k_2 v^{1/2} \quad (3)$$

The *b* values of MnO redox peaks are calculated by CV curve (Fig. S8a in Supporting information). Fig. S8b (Supporting information) shows the *b* values of redox peaks in MnO are 0.50 and 0.79, suggesting that diffusion behavior dominates electrochemical process of MnO. The capacitive contribution rate of MnO at a scan rate of 0.3 mV/s is 44.25% (Fig. S8c in Supporting information), and capacitive proportion increases from 44.25% to 63.87% as the scan rate increases from 0.3 mV/s to 1.5 mV/s. The *b* values (0.84/0.69/0.69/0.80) and capacitive contribution rate (44.20%, 47.13%, 49.47%, 60.60%, 62.50%) of MnV_2O_4 are calculated by the same method in Fig. S9 (Supporting information).

To explore the Zn^{2+} storage mechanism and structural changes of NM700 cathode, *ex-situ* XRD was conducted at different states of the first two charge and discharge processes (Fig. 4e). After the initial discharge, XRD pattern of NM700 electrode remains almost unchanged, except for a slight shift of the (311) peak of MnV_2O_4 and (111) peak of MnO around 35° towards lower angles, which is attributed to the interlayer spacing expansion caused by the insertion of Zn^{2+} [48]. Subsequently, the above peaks move back to higher angles during the first charging process, reflecting that the structure of NM700 is recovered after Zn^{2+} extraction (Fig. S10 in Supporting information) [46]. It is also observed that (333) peak of MnV_2O_4 around 56° towards higher angles in Fig. S10. Interestingly, small peaks appear near 12.3° and 17° at the first discharge to 0.2 V, corresponding to the (001) and (100) plane of $Zn_3(OH)_2V_2O_7{\cdot}2H_2O$ (ZVO), respectively. Fig. S11 (Supporting information) shows that there are obvious ZVO diffraction peaks on the surface of NM700 after 2000th cycles at 10 A/g, further indicating a conversion reaction occurred and the formation of ZVO, and ZVO is coexisted with NM700 during subsequent charge and discharge processes [46].

In summary, MnO/MnV_2O_4 heterostructure cathode material has been successfully prepared by hydrothermal method followed by the calcination process. Benefiting from the synergistic effect of heterostructure combining the advantages of MnO and MnV_2O_4, as a result, the specific capacity of NM700 is up to 342 mAh/g at 0.1 A/g, and the capacity is decreased by only 23% while the current density increases 150 times (261 mAh/g at 15 A/g). The MOF framework ensures the structural stability of NM700, so the specific capacity can be maintained at 198.9 mAh/g after 2000th cycles of 10 A/g (81.0%). Consequently, this work can be expected to inspire the development of other advanced aqueous ion-types energy storage devices in future energy applications.

Declaration of competing interest

The authors declare that they have no known competing financial interests or personal relationships that could have appeared to influence the work reported in this paper.

Acknowledgments

This work was supported by the Key Projects of Intergovernmental International Cooperation in Key R & D Programs of the Ministry of Science and Technology of China (No. 2021YFE0115800), the National Science Funding Committee of China (No. U20A20250).

Supplementary materials

Supplementary material associated with this article can be found, in the online version, at doi:10.1016/j.cclet.2023.109326.

References

[1] N. Zhang, J.C. Wang, Y.F. Guo, et al., Coord. Chem. Rev. 479 (2023) 215009.
[2] L.E. Blanc, D. Kundu, L.F. Nazar, Joule 4 (2020) 771–799.
[3] Y. Ding, L. Zhang, X. Wang, et al., Chin. Chem. Lett. 34 (2023) 107399.
[4] J. Yan, E.H. Ang, Y. Yang, et al., Adv. Funct. Mater. 31 (2021) 2010213.
[5] X. Wu, C. Yin, M. Zhang, et al., Chem. Eng. J. 452 (2023) 139573.
[6] F. Wu, B. Wu, Y. Mu, et al., Int. J. Mol. Sci. 24 (2023) 6041.
[7] H. Liu, J.G. Wang, Z. You, et al., Mater. Today 42 (2021) 73–98.
[8] Q. Wen, H. Fu, R.D. Cui, et al., J. Energy Chem. 83 (2023) 287–303.
[9] J. Ming, J. Guo, C. Xia, W. Wang, H.N. Alshareef, Mat. Sci. Eng. R 135 (2019) 58–84.

[10] K.Y. Zhang, Z.Y. Gu, E.H. Ang, et al., Mater. Today 54 (2022) 189–201.
[11] Z.X. Huang, X.L. Zhang, X.X. Zhao, et al., Sci. China Mater. 66 (2022) 79–87.
[12] X. Zhao, X. Liang, Y. Li, Q. Chen, M. Chen, Energy Storage Mater 42 (2021) 533–569.
[13] F. Tang, X. Wu, Y. Shen, et al., Energy Storage Mater. 52 (2022) 180–188.
[14] K. Cai, S.H. Luo, J. Feng, et al., Chem. Rec. 22 (2022) e202100169.
[15] X. Zhang, J.P. Hu, N. Fu, et al., InfoMat 4 (2022) e12306.
[16] T. Lv, Y. Peng, G. Zhang, et al., Adv. Sci. 10 (2023) e2206907.
[17] J. Yang, B. Yin, Y. Sun, et al., Nano-Micro Lett. 14 (2022) 42.
[18] G. Li, L. Sun, S. Zhang, et al., Adv. Funct. Mater. 34 (2024) 2301291.
[19] T. Zhou, L. Zhu, L. Xie, et al., J. Colloid Interf. Sci. 605 (2022) 828–850.
[20] N. Zhang, Y.R. Ji, J.C. Wang, et al., J. Energy Chem. 82 (2023) 423–463.
[21] L. Li, S. Jia, Z. Cheng, C. Zhang, Nanoscale 15 (2023) 9589–9604.
[22] T. Zhao, H. Wu, X. Wen, et al., Coord. Chem. Rev. 468 (2022) 214642.
[23] J. Yang, R. Zhao, Y. Wang, et al., Adv. Funct. Mater. 33 (2023) 2213510.
[24] Y. Shang, D. Kundu, Curr. Opin. Electrochem. 33 (2022) 100954.
[25] W. Yang, W. Yang, Y. Huang, et al., Chin. Chem. Lett. 33 (2022) 4628–4634.
[26] Y. Liu, Y. Liu, X. Wu, Chin. Chem. Lett. 34 (2023) 107839.
[27] Y. Li, J. Zhao, Q. Hu, T. Hao, et al., Mater. Today Energy 29 (2022) 101095.
[28] Z.Y. Gu, Y.L. Heng, J.Z. Guo, et al., Nano Res. 16 (2022) 439–448.
[29] X. Guo, G. He, J. Mater. Chem. A 11 (2023) 11987–12001.
[30] X. Tang, D. Zhou, B. Zhang, et al., Nat. Commun. 12 (2021) 2857.
[31] Y. Liu, X. Wu, Chin. Chem. Lett. 33 (2022) 1236–1244.
[32] S. Lee, J. Hwang, W.J. Song, S. Park, Batteries Supercaps 5 (2022) e202200237.
[33] X. Li, H. Cheng, H. Hu, et al., Chin. Chem. Lett. 32 (2021) 3753–3761.
[34] Q.N. Zhu, Z.Y. Wang, J.W. Wang, et al., Rare Metals 40 (2020) 309–328.
[35] X. Gao, Y. Li, W. Yin, X. Lu, Chem. Rec. 22 (2022) e202200092.
[36] A. Zhang, R. Zhao, Y. Wang, et al., Energy Environ. Sci. 16 (2023) 3240–3301.
[37] S. Wang, Z. Sang, X. Zhao, et al., Batteries Supercaps 5 (2021) e202100313.
[38] Z. Zhang, W. Li, Y. Shen, et al., J. Energy Storage 45 (2022) 103729.
[39] X. Wu, G. Liu, S. Yang, et al., Chin. Chem. Lett. 34 (2023) 107540.
[40] L. Ou, H. Ou, M. Qin, et al., ChemSusChem 15 (2022) e202201184.
[41] Y. Zhang, A. Chen, J. Sun, J. Energy Chem. 54 (2021) 655–667.
[42] L. Cheng, J. Chen, Y. Yan, et al., Chem. Phys. Lett. 778 (2021) 138772.
[43] M. Singha, R.K. Yadav, S. Choudhary, C. Kapoor, R. Gupta, Mater. Today Commun. 35 (2023) 105602.
[44] H. Chen, P. Lv, P. Tian, et al., J. Energy Chem. 82 (2023) 248–258.
[45] K. Sun, J. Pang, Y. Zheng, et al., J. Alloy Compd. 923 (2022) 166470.
[46] W. Leng, L. Cui, Y. Liu, Y. Gong, Adv. Mater. Interf. 9 (2021) 2101705.
[47] S. Wei, S. Chen, X. Su, et al., Energ. Environ. Sci. 14 (2021) 3954–3964.
[48] W. Li, X. Gao, Z. Chen, et al., Chem. Eng. J. 402 (2020) 125509.